Monthly Notices
of the
ROYAL ASTRONOMICAL SOCIETY

Mon. Not. R. Astron. Soc. **416,** 1723–1738 (2011) doi:10.1111/j.1365-2966.2011.18789.x

Galactic winds and extended Lyα emission from the host galaxies of high column density quasi-stellar object absorption systems

Luke A. Barnes,[1⋆] Martin G. Haehnelt,[2] Edoardo Tescari[3,4,5] and Matteo Viel[3,4]

[1]*Institute for Astronomy, ETH Zurich, Wolfgan-Pauli-Strasse 27, CH-8093 Zurich, Switzerland*
[2]*Institute of Astronomy and Kavli Institute for Cosmology, Madingley Road, Cambridge CB3 0HA*
[3]*INAF – Osservatorio Astronomico di Trieste, Via G.B. Tiepolo 11, I-34131 Trieste, Italy*
[4]*INFN/National Institute for Nuclear Physics, Via Valerio 2, I-34127 Trieste, Italy*
[5]*Dipartimento di Fisica - Sezione di Astronomia, Universitá di Trieste, Via G.B. Tiepolo 11, I-34131 Trieste, Italy*

Accepted 2011 March 24. Received 2011 March 22; in original form 2010 December 20

ABSTRACT

We present three-dimensional (3D) resonant radiative transfer simulations of the spatial and spectral diffusion of the Lyα radiation from a central source in the host galaxies of high column density absorption systems at $z \sim 3$. The radiative transfer simulations are based on a suite of cosmological galaxy formation simulations which reproduce a wide range of observed properties of damped Lyα absorption systems. The Lyα emission is predicted to be spatially extended up to several arcsec, and the spectral width of the Lyα emission is broadened to several hundred (in some case more than thousand) km s^{-1}. The distribution and the dynamical state of the gas in the simulated galaxies are complex, the latter with significant contributions from rotation and both in- and out-flows. The emerging Lyα radiation extends to gas with column densities of $N_{\rm H\,I} \sim 10^{18}$ cm^{-2} and its spectral shape varies strongly with viewing angle. The strong dependence on the central H I column density and the H I velocity field suggests that the Lyα emission will also vary strongly with time on time-scales of a few dynamical times of the central region. Such variations with time should be especially pronounced at times where the host galaxy undergoes a major merger and/or starburst. Depending on the pre-dominance of in- or out-flow along a given sightline and the central column density, the spectra show prominent blue peaks, red peaks or double-peaked profiles. Both spatial distribution and spectral shape are very sensitive to details of the galactic wind implementation. Stronger galactic winds result in more spatially extended Lyα emission and – somewhat counterintuitively – a narrower spectral distribution.

Key words: galaxies: formation – quasars: absorption lines.

1 INTRODUCTION

Searches for Lyα emission that are performed down to very low flux levels can detect very faint objects where the Lyα emission is little affected by dust. Lyα emission has therefore developed into an important tool to study high-redshift galaxies (Cowie & Hu 1998; Steidel et al. 2000; Hu et al. 2002; Kodaira et al. 2003; Rhoads et al. 2004; Taniguchi et al. 2005; Kashikawa et al. 2006; Iye et al. 2006; Stanway et al. 2007; Ota et al. 2008; Ouchi et al. 2010). At high redshift, or for intrinsically faint objects, it is also often the only means of establishing a spectroscopic redshift. At low flux levels, Lyα emission due to star formation in galaxies can be spatially very extended due to the resonant scattering of Lyα photons – even if Lyα cooling is not important and the corresponding continuum emission is very compact (Hayashino et al. 2004; Dijkstra, Haiman & Spaans 2006; Rauch et al. 2008, hereafter R08; Finkelstein et al. 2010).

Deep Lyα observations of the high-redshift Universe thus have tremendous potential to probe the surrounding neutral gas in protogalaxies, and thereby shed light on the galaxy formation. The spectroscopic survey of R08 for low surface brightness Lyα emitters based on a 92 h long exposure with the European Southern Observatory VLT FORS2 instrument has pushed Lyα surveys to new sensitivity limits and yielded a sample of 27 spatially extended (several arcsec) low-surface Lyα emitters with fluxes of 3×10^{-18} erg s^{-1} cm^{-1} and a space density of $\sim 3 \times 10^{-2}\, h_{70}^3$ Mpc^{-3}, similar to that of the faintest dwarf galaxies in the local Universe. Based on the inferred incidence rate for absorption, R08 argued that their sample should overlap significantly with the elusive host population of Damped Lyα Absorption Systems (DLAs).

Barnes & Haehnelt (2009, 2010, hereafter BH09 and BH10, respectively), building on the successful model for DLAs of Haehnelt,

⋆E-Mail: luke.barnes@phys.ethz.ch

Steinmetz & Rauch (1998, 2000), presented a simple model that simultaneously accounts for the kinematic properties, column density distribution and incidence rate of DLAs *and* the luminosity function and the size distribution of the R08 emitters in the context of the Λcold dark matter model for structure formation. The modelling of BH10 assumed spherical symmetry and simple power-law profiles for gas density and peculiar velocity. Lyα radiative transfer is, however, sensitive to the details of the spatial distribution and velocity of H I – inhomogeneity can provide channels for rapid spatial diffusion, while bulk velocities have a similar effect in frequency space.

The complicated physics of galaxy formation – gravity, hydrodynamics, radiative cooling, star formation, supernovae, galactic winds, ionizing radiation, metal and dust production – has led to numerical simulations being the method of choice for investigating the physical properties of the gas from which galaxies form. These simulations provide us with realistic three-dimensional (3D) density and velocity fields that take into account most of the relevant physics.

Here, we will apply the Lyα radiative transfer code developed in BH10, adapted for the post-processing of 3D gas distributions, to the results of a simulation of DLA host galaxies in a cosmological context by Tescari et al. (2009). We study the effect of the spatial distribution and the kinematic state of the H I on the low surface brightness spatially extended Lyα emission, which should become an important probe of kinematics of the gas in DLA host galaxies.

In this first paper, we will focus on a detailed investigation of a small number of such simulated systems. In Section 2, we describe the (minor) changes to our Lyα radiative transfer code needed to follow photons through a density distribution on a 3D grid. In Section 3.1, we describe the set of simulations of Tescari et al. (2009) that we have used, and in Section 3.2 we describe the three haloes that we have extracted from the simulations for further study. Section 4 discusses the haloes in detail, looking particularly at the effect of galactic winds on the gas properties and Lyα emission. We discuss our results in Section 5, including their relevance to observed populations of high-redshift Lyα emitters, including Lyman Break Galaxies (LBGs), before presenting our conclusions in Section 6.

2 THE 3D Lyα RADIATIVE TRANSFER CODE

The 3D Lyα cosmological radiative transfer of Lyα radiation has been studied by a number of authors (Cantalupo et al. 2005; Tasitsiomi 2006; Laursen, Razoumov & Sommer-Larsen 2009a; Zheng et al. 2010; Kollmeier et al. 2010; Faucher-Giguère et al. 2010; Zheng et al. 2011), in the context of, for example, fluorescent emission from the intergalactic medium (IGM), bright Lyα emitters at $z \approx 8$, young LBGs and Lyα emission linked to radiative cooling.

We have previously described our implementation of a 1D Lyα radiative transfer algorithm in BH10. In short, Lyα photons are created according to the emissivity profile, and then propagated through the gas. Each time the photon is scattered, a new frequency is calculated by assuming that the photon's frequency in the scattering atom's frame is unchanged. Thus, the code tracks the random walk in both real and frequency space before the photon escapes and is observed. The new code used here follows photons through a regular 3D grid. The acceleration scheme, by which photons which have frequencies close to line centre are scattered into the wings, is adapted to the conditions in the current cell. We have tested and subsequently adopted a prescription similar to that described in Laursen et al. (2009a). Further details on the code can be found in Barnes (2010).

The emergent spectrum will depend on the angle from which the system is viewed. Rather than 'waiting' for enough photons to emerge in a given direction, we implement the 'peeling-off' algorithm, described in Yusef-Zadeh, Morris & White (1984) and Wood & Reynolds (1999). At each scattering, the probability of escape in the direction of the observer is calculated and a suitable weight added to the corresponding 2D pixel. The photons that eventually escape the system are used to calculate the angularly averaged spectrum and surface brightness profile. We have run standard test problems to test our 3D code and found that they are reproduced very well.

Our modelling nevertheless has a number of significant simplifications. We post-process the output of cosmological simulations. The simulations therefore do not take into account the dynamical effect of radiation pressure. Lyα radiation pressure has been proposed to provide sufficient energy to launch an outflowing supershell for luminous sources (Dijkstra & Loeb 2009a). However, the systems that we consider here do not have the necessary Lyα luminosity for radiation pressure to be dynamically significant. Our simulations also ignore the evolution of the density and velocity field over the light traveltime of the Lyα photons. We further only consider a very centrally concentrated emissivity. For simplicity we inject photons at the centre of mass of the halo. The photons are created with line-centre frequency in the fluid frame of the gas. We will discuss these assumptions further in Section 5.1.

3 Lyα RADIATIVE TRANSFER IN DLA HOST GALAXIES

3.1 The simulations of DLA host galaxies in a cosmological context by Tescari et al.

We make use of the cosmological hydrodynamic simulations described in Tescari et al. (2009). These simulations were aimed at reproducing the physical properties of the host galaxies of DLAs at $z \sim 3$. The numerical code is a modification of GADGET-2, which is a parallel Tree-PM SPH code (Springel 2005). The code is extensively described in Tornatore et al. (2007), where it was used to simulate clusters of galaxies (see also Tornatore et al. 2010 and Tescari et al. 2011). In addition to gravity and hydrodynamics, the other physical processes that are modelled in the simulation are as follows.

(i) Radiative cooling and heating, including a UV background produced by quasars and galaxies.

(ii) Chemical evolution, using the model of Tornatore et al. (2007) which traces the following elements: H, He, C, O, Mg, S, Si and Fe. The contribution of metals is included in the cooling function. The release of metals from Type Ia and Type II supernovae, as well as low- and intermediate-mass stars, is followed.

(iii) An effective model for the interstellar medium (ISM) (Springel & Hernquist 2003), whereby a gas particle is flagged as star forming whenever its density exceeds a critical threshold. Star-forming particles are treated as multiphase, being a mixture of stars and the cold clouds from which they form. The neutral hydrogen fraction depends on the UV background in the low-density gas, and on the fraction f_c of mass in cold clouds above the density threshold.

(iv) Galactic winds, using two different prescriptions. An energy-driven wind model is implemented in the form of a fixed velocity

Table 1. Characteristic properties of three DM haloes of DLA host galaxies.

Halo ID	Wind model	Mass ($M_\odot$)	Mass H I ($M_\odot$)	Virial velocity ($km\,s^{-1}$)	Virial radius (kpc)	Virial radius (arcsec)	Lyα luminosity ($\times 10^{40}$ erg s^{-1})
1	Momentum (MDW)	7.70×10^{11}	2.03×10^{10}	206.7	77.5	9.8	882.7
	Strong (SW)	7.24×10^{11}	1.38×10^{10}	202.5	76.0	9.6	830.9
	Weak (WW)	8.15×10^{11}	2.80×10^{10}	210.7	79.0	10.0	935.3
	None (NW)	8.12×10^{11}	2.00×10^{10}	210.4	78.9	10.0	931.5
2	MDW	1.54×10^{11}	3.36×10^{9}	120.9	45.3	5.8	176.5
	SW	1.40×10^{11}	1.07×10^{9}	117.2	43.9	5.6	160.8
	WW	1.70×10^{11}	6.22×10^{9}	125.0	46.9	5.9	195.1
	NW	1.65×10^{11}	4.76×10^{9}	123.7	46.4	5.9	189.3
3	MDW	1.46×10^{10}	2.74×10^{8}	55.1	20.7	2.6	16.7
	SW	1.36×10^{10}	1.30×10^{8}	53.8	20.2	2.6	15.6
	WW	1.58×10^{10}	8.10×10^{8}	56.6	21.2	2.7	18.2
	NW	1.57×10^{10}	9.12×10^{8}	56.5	21.2	2.7	18.1

kick given to a chosen particle, with a mass-loss rate proportional to the star formation rate. Tescari et al. (2009) also investigated a Momentum Driven Wind (MDW) model that mimics a scenario in which the radiation pressure of a starburst drives an outflow. In this model, the velocity kick scales with the velocity dispersion of the galaxy. These wind prescriptions are admittedly rather crude, and rely on phenomenological parameters that are poorly constrained either by observations or by more sophisticated modelling. This reflects the significant uncertainty regarding the influence of winds on galaxy formation.

Tescari et al. (2009) investigated simulations with varying box size and numerical resolution for a range of different implementations of galactic winds. Their fiducial simulation employed a strong wind (SW), and the following simulation parameters:[1] $10\,h^{-1}$ Mpc box size (comoving), 320^3 particles, mass resolution $3.5 \times 10^5\,h^{-1}\,M_\odot$ and $1.5\,h^{-1}$kpc (comoving) gravitational softening length. Resolution tests using varied box sizes and particle numbers confirmed that the parameters of the fiducial simulation were sufficient to ensure convergence for all the quantities of interest.

The SW simulation employed a strong (600 $km\,s^{-1}$), energy-driven wind and a Salpeter stellar initial mass function (IMF). Looking ahead to a favourable comparison with the R08 emitters in a later section, we will instead focus more on the MDW simulation, which differs from the SW simulation only in the wind implementation. We will compare the results of both the MDW and SW simulation with two further simulations: a weak (energy-driven, 100 $km\,s^{-1}$) wind (WW) and a simulation with no wind (NW) which did not appear in Tescari et al. (2009). As we will see, the MDW and the SW simulations are somewhat similar, as are the WW and NW simulations.

The simulations of Tescari et al. (2009) reproduce most observed properties of DLAs rather well. The observed incidence rate of DLAs is matched by the simulations, assuming that haloes below $10^9\,h^{-1}\,M_\odot$ do not host DLAs. The observed column density distribution is also reproduced successfully for the SW and MDW simulations, while the total neutral gas mass in DLAs ($\Omega_{\rm DLA}$) is reproduced for MDW but underpredicted by a factor of about 1.7 at $z = 3$ in the SW simulation. The most problematic observable is the velocity width distribution of low-ionization associated metal absorption. The high-velocity tail of the distribution is significantly underpredicted in all simulations. The simulations do not produce enough absorption systems with velocity width greater than 100 $km\,s^{-1}$. This is a common problem for numerical simulations of DLA host galaxies (Pontzen et al. 2008; Razoumov et al. 2008), but see Hong et al. (2010) and Cen (2010) which appear to be somewhat more successful in this respect. We will come back to this point later.

[1] The cosmological parameters employed by both Tescari et al. (2009) and this work are: $(h, \Omega_{\rm M}, \Omega_{\rm b}, \Omega_\Lambda, \sigma_8, n) = (0.73, 0.24, 0.0413, 0.76, 0.8, 0.96)$.

3.2 Three representative haloes

We have selected three haloes at $z = 3$ from the simulations for a detailed study. Some basic properties of the haloes are summarized in Table 1. The virial velocity and radius are calculated from the mass of the particles grouped by the halo finder (see Maller & Bullock 2004 for the relevant formulae). Note that the properties of a given halo for the different wind model simulations are very similar. The final column lists the Lyα luminosity ($L_{\rm Ly\alpha}$), calculated following BH09 and BH10, as

$$L_{\rm Ly\alpha} = 10^{42} \left(\frac{v_{\rm c}}{100\,{\rm km\,s^{-1}}} \right)^3 {\rm erg\,s^{-1}}, \quad (1)$$

where $v_{\rm c} \propto M^{1/3}$ is the virial velocity of the halo. With this choice BH09 and BH10 were able to reproduce the luminosity function of the R08 emitters. The masses of the three haloes probe the range of masses predicted to contribute significantly to the incidence rate of DLAs/emitters per unit log mass ($\mathrm{d}^2\mathcal{N}/\mathrm{d}X/\mathrm{d}\log_{10} M$). The corresponding luminosities span the range of those observed in the survey of R08.

The physical properties of these haloes (neutral hydrogen density, temperature and bulk velocity) were projected on to a regular 3D grid centred on the centre of mass of the halo. The cubes containing Haloes 1 and 2 have 128^3 cells, each with side length $3.125\,h^{-1}$ comoving kpc, making the entire cube $400\,h^{-1}$ comov.kpc across. The cube containing Halo 3 has 64^3 cells, each also $3.125\,h^{-1}$ comov.kpc across, making the width of the entire cube $200\,h^{-1}$ comov.kpc.

We will first examine the simulation with the MDW implementation of galactic winds, before comparing with the other simulations in later sections. Fig. 1 shows the angularly averaged radial mass flow rate, projected column density of neutral hydrogen and the Lyα

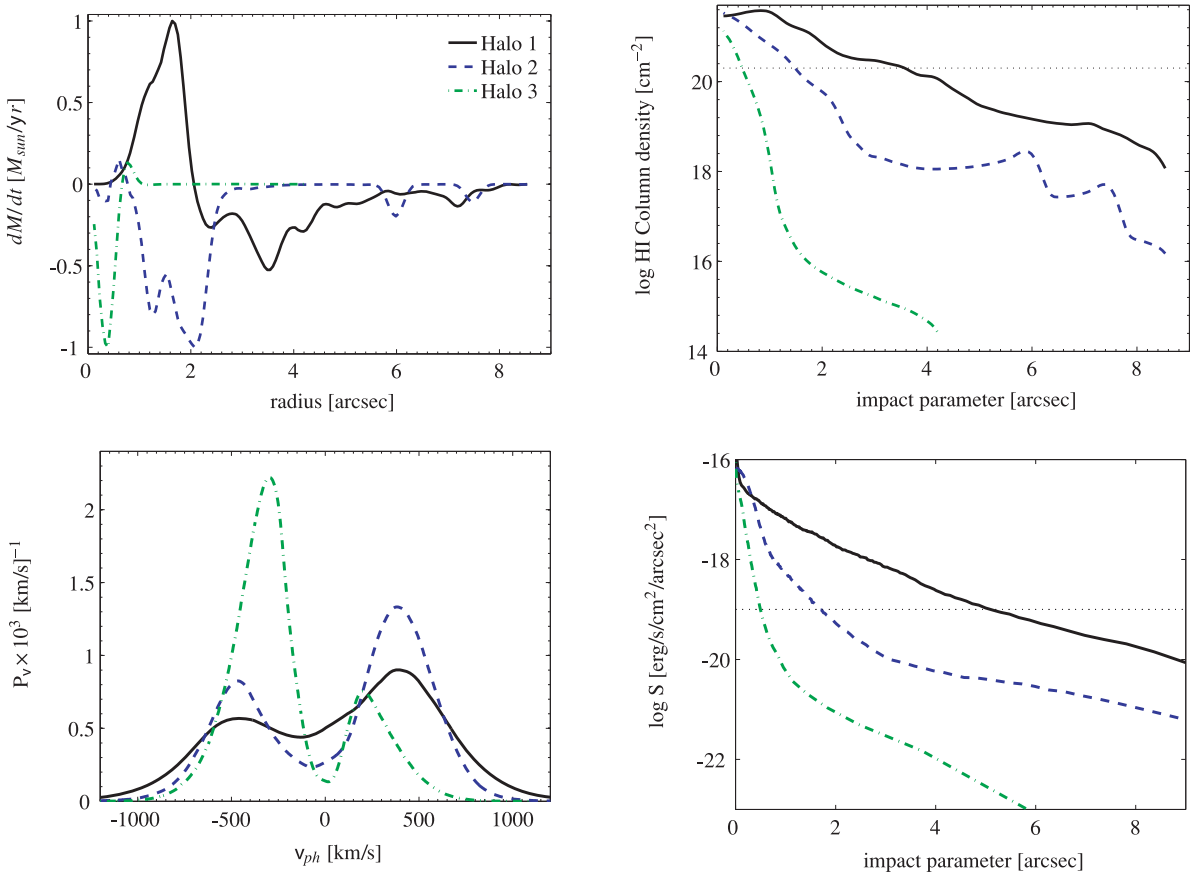

Figure 1. The angularly averaged properties of the three DLA host galaxies described in Table 1, for the MDW wind model. The upper-left panel shows dM/dt, which is the rate at which H I mass is flowing through a surface of constant radius r, normalized to a maximum $|\dot{M}| = 1$. The maximum $\dot{M}$ (by which the curve are scaled) are 97, 8.5 and 1.5 $M_\odot yr^{-1}$, for Haloes 1, 2 and 3, respectively. The upper-right panel shows the average column density for a sightline passing at a given impact parameter from the centre of the halo. The thin dotted horizontal line indicates the minimum column density of a DLA, $N_{\rm DLA} = 10^{20.3}\,{\rm cm}^{-2}$. The lower-left panel shows the (observed) angularly averaged spectrum, with the area under each curve normalized to unity. The lower-right panel shows the surface brightness profile; the horizontal line shows the surface brightness limit of the R08 survey. The assumed total Lyα luminosities (which normalize each curve) are given in the last column of Table 1.

surface brightness as a function of radius/impact parameter as well as the angularly averaged spectral shape of the Lyα emission for the three haloes.

The rate at which H I mass flows through a surface of constant radius r is shown in the upper-left panel of Fig. 1, normalized to a maximum $|\dot{M}| = 1$. Positive (negative) values correspond to outflow (inflow). The maximum $\dot{M}$ is 97, 8.5 and 1.5 $M_\odot\,yr^{-1}$, for Haloes 1, 2 and 3, respectively. Note that, for the MDW implementation shown here, only in the most massive halo does the wind actually manage to globally reverse the gravitational infall. The mass flow shows a mixture of inflow and outflow, with inflow often dominating in the outer parts of the halo.

The upper-right panel of Fig. 1 shows the average column density for a sightline passing at a given impact parameter from the centre of the halo. The thin dotted horizontal line indicates the minimum column density of a DLA, $N_{\rm DLA} = 10^{20.3}\,{\rm cm}^{-2}$. As expected, the column density peaks near the centre of the halo. The 'steps' in the column density profiles of Haloes 2 and 3 show the influence of separate clumps of H I at large radii. The neutral hydrogen column density exceeds the threshold for a DLA, which extends to a radius of 3.5, 1.5 and 0.5 arcsec, respectively.

The lower-left panel shows the (observed) angularly averaged spectrum, with each curve normalized to unity. The lower-right panel shows the surface brightness profile. The luminosity used to normalize each curve is given in the last column of Table 1.

The surface brightness profiles peak at the centre of the halo, and generally follow the decline of the column density whilst being much smoother. The Lyα emission is scattered to similarly large radii as in the observed emitters. The haloes are surrounded by low surface brightness emission which extends to radii of several arcsec. The size of the emitter, as measured to the surface brightness limit of the R08 (shown by the horizontal dotted line), is generally larger than the cross-section for damped absorption. The more massive haloes are more spatially extended, while the smaller haloes display a more pronounced central peak.

The angularly averaged spectrum of the most massive halo is fairly symmetric with well-separated blue and red peaks. The red peak is slightly stronger. The two low-mass haloes have a more clearly dominant red and blue peak, respectively. Increasing central column density clearly leads to more diffusion in frequency space. We will see in the next section that the spectral shape varies strongly between different directions and that there is a correlation between the dominance of inflow (outflow) and the domination of the blue

(red) peak in the spectrum. We will leave a more detailed discussion until then.

4 THE EFFECT OF GALACTIC WINDS ON Lyα EMISSION

We will now discuss the simulations of the intermediate-mass halo (our fiducial Halo 2) in more detail with particular emphasis on the effect of galactic winds on the physical properties of the gas in the halo and on the emission properties of the Lyα emission. Halo 2 has a mass of about $1.5 \times 10^{10}\,\mathrm{M}_{\odot}$ and a virial velocity of about $120\,\mathrm{km\,s^{-1}}$. Its properties are similar to the brightest of the emitters in the R08 survey, and its mass coincides with the peak of our preferred model for the DLA mass function ($\mathrm{d}^2\mathcal{N}/\mathrm{d}X/\mathrm{d}\log_{10} M$) from BH10 and thus should represent a typical DLA host galaxy.

4.1 Angularly averaged properties

Angularly averaged properties of simulation based on Halo 2 for each of the wind models are shown in Fig. 2. The legend in the top-right panel shows the line-styles of the different wind models.

The top-left panel shows the H I number density as a function of radius. Note that the average cosmic number density of hydrogen at $z \approx 3$ is $1.2 \times 10^{-5}\,\mathrm{cm^{-3}}$, while the volume-averaged neutral fraction of hydrogen in the IGM is $\lesssim 10^{-5}$. A small decrease in the number density at small radii is the result of the centre of mass of the neutral hydrogen being offset from the centre of mass of the halo. The number density profile shows the effect of several clumps of H I. The most dramatic difference between the models is in the centre of the haloes, where the presence of a SW can reduce the gas density substantially.

The top-right panel shows the averaged column density for a sightline passing at a given impact parameter from the centre of the halo. The thin dotted horizontal line indicates the minimum column density of a DLA. The column density is a decreasing function of radius, with sightlines containing DLAs probing the centre of the halo. The 'clumps' noticeable in the number density distribution cause steps in the angle-averaged column density distribution and contribute to the Lyman-Limit System cross-section.

The next panel (row 2, column 1) shows the (H I) density-weighted radial velocity profile,

$$v_{\mathrm{H\,I}}(r) \equiv \langle \boldsymbol{v}_{\mathrm{b}} \cdot \hat{\boldsymbol{r}} \rangle \equiv \frac{\int_0^{2\pi}\int_0^{\pi} (\boldsymbol{v}_{\mathrm{b}} \cdot \hat{\boldsymbol{r}}) \rho_{\mathrm{H\,I}}(r,\theta,\phi) \sin\theta \,\mathrm{d}\theta\,\mathrm{d}\phi}{\int_0^{2\pi}\int_0^{\pi} \rho_{\mathrm{H\,I}}(r,\theta,\phi)\sin\theta\,\mathrm{d}\theta\,\mathrm{d}\phi}. \quad (2)$$

The plot reveals the presence of a mixture of inflow (v_{r} negative) and outflow, with the innermost parts of the halo tending to show outflow for the stronger winds (SW and MDW), and inflow for the weaker winds (WW and NW).

The typical velocities of inflow are 50–100 $\mathrm{km\,s^{-1}}$, with the largest velocities being comparable to the virial velocity. There is a general trend towards lower velocities in the centre of the halo. The velocity profile is, however, far from smooth. The total velocity of the gas ($v = \sqrt{\langle |\boldsymbol{v}_{\mathrm{b}}|^2 \rangle}$), by comparison, varies between 100 and 150 $\mathrm{km\,s^{-1}}$ for the stronger winds, and 140 and 200 $\mathrm{km\,s^{-1}}$ for the weaker winds, with a very slight preference for larger velocities at the centre of the halo.

The panel to the right shows the volume-weighted radial velocity profile (v_{V}). For the diffusion of Lyα photons, volume-weighted velocities are actually more relevant than density/mass-weighted velocities as the photons tend to find low-density paths of escape, and so the velocity in the underdense regions is as important or more important as that in high-density regions. We see a clear difference in v_{V} between the stronger and weaker wind models. The SW models have outflows that dominate the kinematics of the gas along most of the escape paths of the photons. For WW models, inflow dominates.

The next panel (row 3, column 1) shows $\mathrm{d}M/\mathrm{d}t$ for H I, which is related to the density-weighted radial velocity as $\mathrm{d}M/\mathrm{d}t = 4\pi r^2 v_{\mathrm{H\,I}}(r)\rho^{\mathrm{av}}_{\mathrm{H\,I}}(r)$, where $\rho^{\mathrm{av}}_{\mathrm{H\,I}}$ is the average neutral hydrogen density at radius r. Notice that the flows in the innermost parts of the halo, while being of modest velocity, carry the most significant amounts of mass.

Comparison of $v_{\mathrm{H\,I}}(r)$, v_{V} and $\mathrm{d}M/\mathrm{d}t$ is quite instructive. The relative smoothness of v_{V} indicates that a small number of dense clumps dominate the mass flow, moving through a relatively smooth background whose kinematics are shaped by the winds. For example, the MDW model (solid black) shows a $\sim$100 $\mathrm{km\,s^{-1}}$ inflowing clump at 2 arcsec that carries a significant amount of mass. However, v_{V} is still positive, showing that the wind is filling the remaining space and outflowing regardless. Lyα photons escaping along low column density paths will generally not 'see' such dense clumps.

The panel to the right shows the rotation velocity of the gas, averaged over *cylindrical* shells, which is approximated as follows. If the gas in the halo were in a rotating disc with a rotation velocity depending only on the cylindrical radius, then the angular momentum within a cylindrical shell R, $R + \mathrm{d}R$ would be

$$|\boldsymbol{L}_{\mathrm{rot}}| = v_{\mathrm{rot}}(R) R \sum_i m_i, \quad (3)$$

where the sum is over the cells inside the shell. Thus for each R, we divide the angular momentum by R times the mass in the shell. As with $v_{\mathrm{H\,I}}(r)$, this distribution is far from smooth due to the influence of dense clumps of gas. The velocity drops from $\sim$150 to $\sim$50 $\mathrm{km\,s^{-1}}$ as we move outwards. The velocity is generally higher in the weaker wind models, possibly indicating that the stronger winds disrupt or delay the settling of gas into a disc. We can also calculate the fraction of the kinetic energy at each radius which is in the form of rotational kinetic energy. This quantity peaks at $\sim$0.7 at the centre of the halo, decreasing to $\sim$0.2 in the outer parts. This shows that the approximations we made in calculating v_{rot} are most accurate at the centre of the halo, as expected.

The bottom-left panel shows the angularly averaged spectrum of the Lyα emission. The thick black curve shows the spectrum as a function of the rest-frame velocity offset ($v_{\mathrm{ph}} \equiv c\Delta\lambda/\lambda_0$). All curves are normalized to have unit area. The weaker wind models show a classic double-peaked profile (Harrington 1973; Neufeld 1990; see also Urbaniak & Wolfe 1981), while the stronger wind models show a more prominent red peak, indicating the influence of the outflowing gas.

We also see that the stronger galactic winds – somewhat counter-intuitively – result in a narrower spectral distribution. This indicates that it is the high central column density, more than the higher outer gas velocities, that is the dominant factor in establishing the typical escape frequency of Lyα photons.

The thick black curve in the bottom-right panel shows the angularly averaged surface brightness profile. The luminosity that normalizes each curve is given in the last column of Table 1. The vertical line indicates the virial radius of the halo, while the horizontal line shows the surface brightness limit of R08. The surface brightness profile shows a central peak with a tail that flattens out as the column density does the same. The emission is more extended in the stronger wind models. There are two reasons for this. The lower central column density means that photons are in general

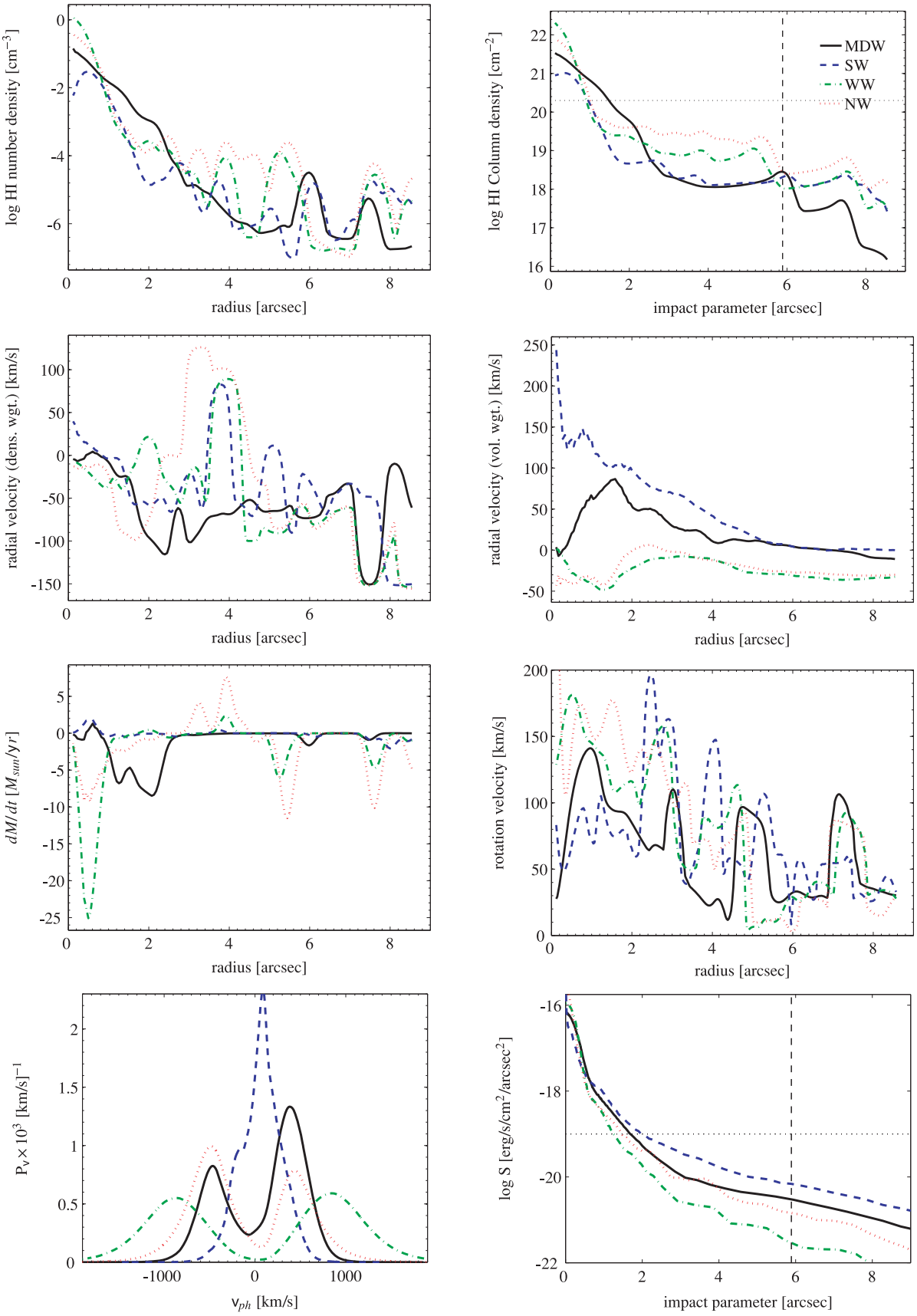

Figure 2. Angularly averaged properties of Halo 2, for the wind prescriptions as shown in the legend (MDW: momentum driven wind, SW: strong wind, WW: weak wind, NW: no wind). The velocities and dM/dt are all for H I. Vertical dashed lines indicate the virial radius. For a detailed discussion, see Section 4.1.

closer to line centre when they encounter the outer parts of the halo, where higher wind velocities can shift the photons sufficiently back towards line centre to be scattered by rather low column density gas. Comparing the radial profile of H I column density and Lyα surface brightness for the different wind models suggests that this is more important than the H I column density in the outer parts of the halo.

We have not plotted the (H I weighted) temperature profile, which for all models decreases gently with radius from around 10^5 to $10^{4.3}$ K. The central temperature is slightly higher in the WW models.

We can now compare the properties of the haloes to the modelling of BH10. Unlike in our previous analytical modelling the column density in our simulations here has a pronounced core at very small radii. At larger radii the radial profile of the H I column density in the MDW model appears rather similar even though much larger samples of simulated haloes would be needed to make a more meaningful comparison [we refer the reader to Tescari et al. (2009) for a quantitative comparison with the observed DLA column density distribution]. The radial velocity profiles in our full cosmological simulations are obviously much more complex than the simple power-law profiles we had assumed in our previous work, although there is a slight trend towards lower velocities at the centre of the halo. There was obviously also no possibility to account for the 3D effects of any clumping in our previous 1D modelling.

4.2 2D views of the halo

Fig. 3 shows maps of the H I column density distribution and Lyα surface brightness and 2D spectra for Halo 2 for the MDW model looking along the x-axis from $-\infty$ (left) and $+\infty$ (right). Note that some of the axes have been flipped so that the left and right columns have their axes pointing in the same direction. The dashed black curve shows the virial radius.

The top panels show the H I column density along a line of sight parallel to the x-axis. Each panel corresponds to a line of sight that passes through the *nearer half of the box*. In other words, the colours in the legend to the right of each figure represent the column density of neutral hydrogen that the photon (emitted at the centre of the halo) would have to pass through if it were to reach the observer directly without any scattering. The solid line in the top two panels is a contour representing $N_{\rm DLA} = 10^{20.3}\,{\rm cm}^{-2}$, calculated for sightlines passing through the *entire* box; it is thus the same in the left and right top panels. A sightline passing through the region inside the contour would encounter a DLA.

The column density distribution reflects the irregular distribution of gas, with a mixture of thin filaments and relatively isolated clumps of neutral hydrogen. The differences between the panels show the asymmetry in the distribution of gas. The cross-section for damped absorption is composed of a large central clump accompanied by a number of isolated clumps, scattered around the halo. The column density of individual clumps of neutral hydrogen drops rapidly below $\sim 10^{17}\,{\rm cm}^{-2}$, due to the effect of the ionizing UV background on particles below the 'cold cloud' threshold.

The next two panels show an image of the halo that is coloured according to the surface brightness of the Lyα emission, calculated[2] assuming the luminosity as described previously and given in Table 1. The solid contour represents the surface brightness limit of the R08 survey, $S_0 = 10^{-19}\,{\rm erg\,s^{-1}\,cm^{-2}\,arcsec^{-2}}$.

The surface brightness maps show that the Lyα emission generally traces but is less clumpy than the underlying neutral hydrogen distribution. In particular, the S_0 contour encloses a much larger area than the DLA contour both by being larger and by having fewer 'holes'. The Lyα photons are scattered effectively out to large radii and lower column densities. The S_0 contour in the surface brightness is roughly similar to that of the $N_{\rm H\,I} \sim 10^{18}\,{\rm cm}^{-2}$ contour[3] in the H I column density plot.

Our central Lyα source is able to illuminate clouds of neutral gas that are detached from the central clump. The Lyα photons tend to find low-density paths of escape. For example, the photons face a column density of H I which is on average approximately seven times larger in the $-z$ direction than in the $+z$ direction, and the corresponding observed Lyα flux is on average approximately three times smaller. For the x direction, as shown in the figure, the difference in the observed flux between two opposite viewpoints is around 70 per cent.

The bottom four panels are 2D spectra, calculated using a 'slit' placed along either the y- or z-direction (labelled in the vertical axis) and with a width of 2 arcsec, the same width as used in R08. The contour shows the spectral intensity limit of the R08 survey, $S_\lambda \approx 4 \times 10^{-20}\,{\rm erg\,s^{-1}\,cm^{-2}\,arcsec^{-2}\,\AA^{-1}}$.

The 2D spectra show a dominant blue peak in the $-x$ direction, and the opposite trend when viewed from $+x$ (see the discussion of Fig. 4). As expected, the separation of the peaks is largest where the column density is largest. The dominance of one peak over the other tends to increase as we look away from the centre of the halo. This is most likely because the probability of a photon scattering in the outer parts of the halo is quite sensitive to the velocity of the gas.

We illustrate the dependence of the emergent spectrum and surface brightness profile on the viewing angle in Fig. 4, which also shows the angularly averaged value (thick black line). The thin coloured lines show the emergent spectrum (calculated by collapsing the slit along its spatial direction, or by averaging over the 2D image) for six different viewpoints along the principal axes. Remember that the observer sees only one of these spectra – the angularly averaged quantities are not observable. The spectra show significant variations, both in which peak dominates and in total amount of light observed. The separation of the peaks shows relatively little variation and the surface brightness profiles are very similar, especially in the outer parts of the halo.

4.3 Haloes 1 and 3

The angularly averaged properties of Halo 1 are shown in Fig. 5. The panels show the volume-averaged radial velocity profile, projected column density of neutral hydrogen, the emergent Lyα spectrum and the Lyα surface brightness as a function of radius/impact parameter. The four different wind models are shown on each plot.

The radial velocity profile shows the effect of the outflowing winds in the low-density gas. The winds provide escape paths filled

[2] See equation (20) of Laursen et al. (2009a).

[3] Varying between $\sim 10^{17}$ and $10^{19}\,{\rm cm}^{-2}$. Note that this is not the same as the mean integrated column density along the final escape flight of the photon, which we have also calculated explicitly using our code and which can be approximated analytically by $N_{\rm esc} \approx 10^{20}\,{\rm cm}^{-2}(v_{\rm peak}/500\,{\rm km\,s}^{-1})^2$, where $v_{\rm peak}$ is the peak of the emission spectrum.

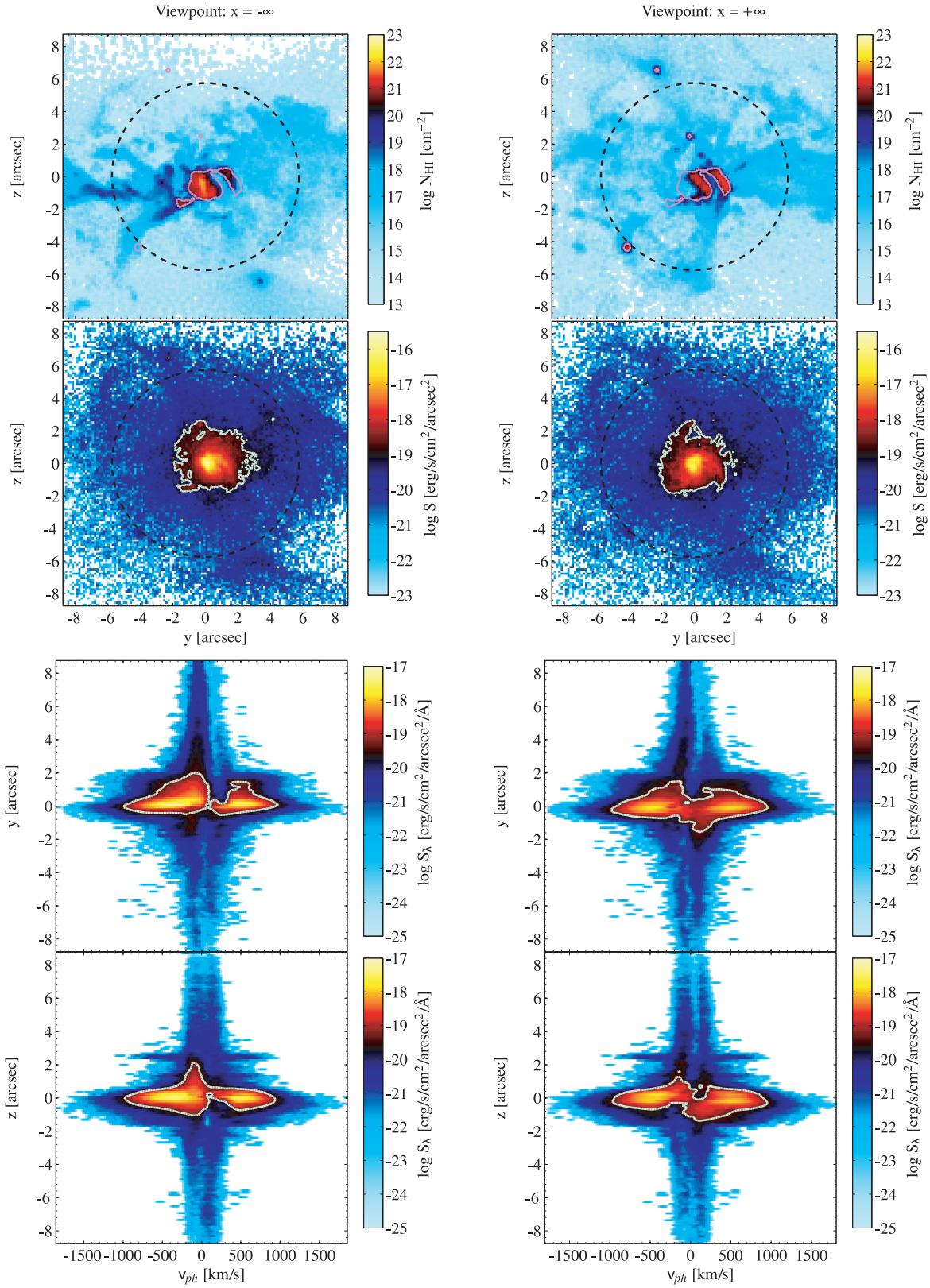

Figure 3. 2D images and spectra for Halo 2 in the MDW simulation. The left (right) column is as viewed from $x = -\infty(+\infty)$. The upper two panels show the H I column density for the *closer half* of the simulation box. The dashed circle shows the virial radius. The contour represents $N_{\rm DLA} = 10^{20.3}$ cm^{-2}, for a sightline passing through the entire box. The next two panels show the observed Lyα surface brightness. The contour shows the surface brightness limit of the R08 survey, $S_0 = 10^{-19}$ erg s^{-1} cm^{-2} arcsec^{-2}. The lower four panels show 2D spectra, calculated using a 'slit' placed along either the y- or z-direction (labelled in the vertical axis) and with a width of 2 arcsec, which is the same width as in R08. The contour shows the spectral intensity limit of the R08 survey (Rauch, private communication), which is $S_\lambda \approx 4 \times 10^{-20}$ erg s^{-1} cm^{-2} arcsec^{-2} Å^{-1}. The figure is discussed further in Section 4.2.

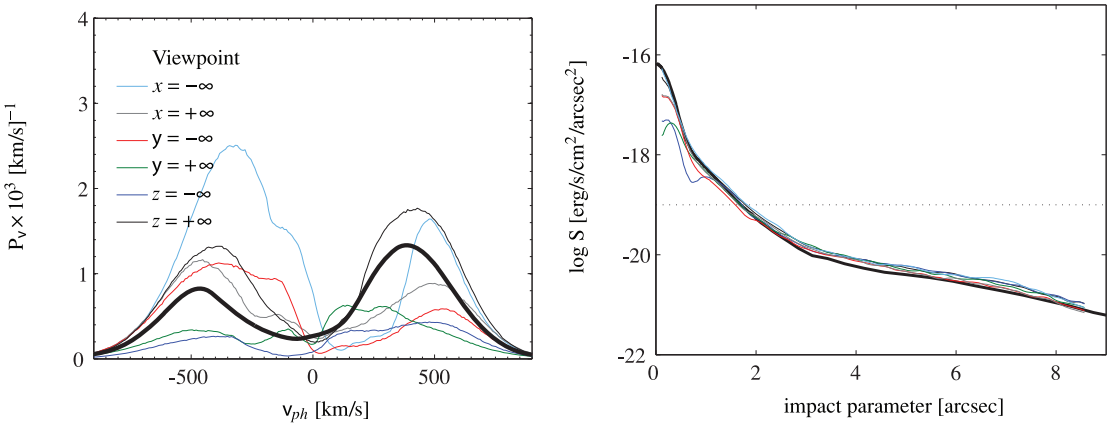

Figure 4. The emergent spectrum (left) and surface brightness profile (right) for Halo 2, showing the effect of the viewing angle. The thick black line is the angularly averaged spectrum, which is the same as in Fig. 1. The thin coloured lines show the emergent spectrum (calculated by collapsing the slit along its spatial direction, or by averaging over the 2D image) for the six different viewpoints as shown in the legend. The figure is discussed further in Section 4.2

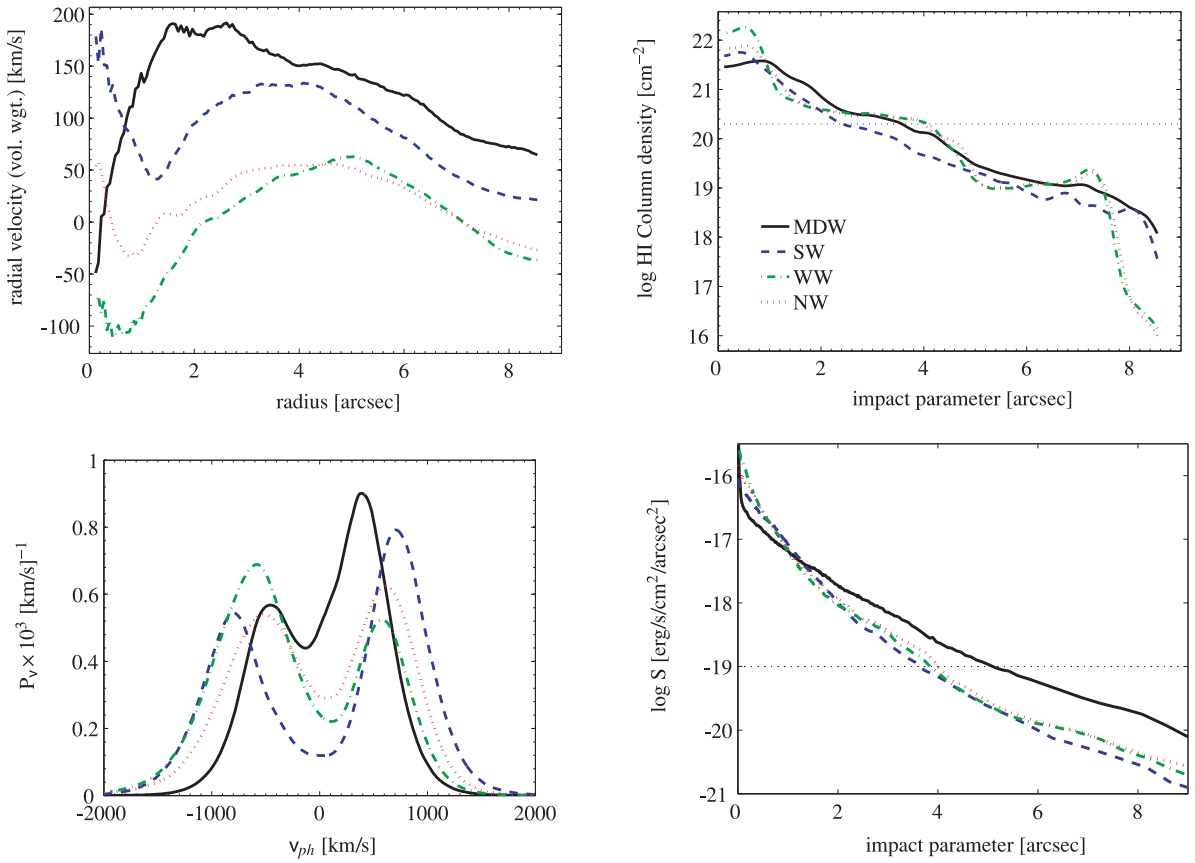

Figure 5. Angularly averaged properties of Halo 1, for the wind prescriptions shown in the legend (upper left), as discussed in Section 4.3. The upper-left panel shows the volume-averaged radial velocity profile. The upper-right panel shows the H I column density as a function of impact parameter. The lower-left panel shows the spectra, normalized to unit area. The lower-right panel shows the surface brightness distribution as a function of impact parameter.

with gas that is outflowing at ∼100–150 km s^{-1}, while in the weaker wind cases the average velocity is closer to zero.[4]

[4] The fact that the volume-averaged radial velocity is slightly positive in the NW simulation is most likely due to the centre of mass of the baryons being offset from the centre of mass of the halo, i.e. the baryons have overshot the bottom of the potential well. Heating of the hot, rarefied ISM by the UVB may also contribute.

The column density profile of Halo 1 is somewhat smoother than that of Haloes 2 and 3, and as expected the DLA cross-section is significantly larger. Once again, we see that the winds have lowered the central column density of the halo.

For Halo 1, the spectra show again the classic double-peaked profile with a general trend towards domination of the red peak for haloes with stronger winds. The surface brightness profiles are rather similar: they peak at the centre, and decrease smoothly as the column density drops. The weaker wind models

are as expected more centrally peaked than the stronger wind models.

The angularly averaged properties of Halo 3 are shown in Fig. 6. The gas in the stronger wind models is more extended. Volume-weighted all of the models are dominated by infall at small radii, with only the SW model showing a very mild outflow at large radii. The MDW wind clearly decreases the average infall rate, but not to the extent that the infall is reversed.

The angularly averaged spectrum of Halo 3 is a particularly nice illustration of inflowing gas at the centre of the halo producing a more prominent blue peak in the spectrum. In spite of this, there are viewing angles for which the spectrum is dominated by a red peak (see Fig. 9). The surface density profile reflects the column density profile – the inner, dense core results in a central peak whose rapid decline gives way to a shallower plateau as we reach the outer, diffuse background.

Figs 7–9 show a comparison of the 2D maps and spectra for the MDW (left) and WW (right) wind prescriptions for the three haloes. Note that the left-hand panel of Fig. 8 is the same as the left-hand panel of Fig. 3, and is reproduced in this figure for convenience. As noted above, the emission is more extended in the stronger wind models, and stronger winds produce a narrower spectral distribution (note the difference in the horizontal scale of the 2D spectra).

5 DISCUSSION

The dependence of the spectra, in both the line shape and the total observed surface brightness, on the viewing angle is very striking and is obviously very important for the interpretation of observed (spatially extended low surface brightness) Lyα emitters. It suggests, e.g., that the large variety of line shapes in the observed sample of R08 is at least partially an orientation effect. The dependence of surface brightness on orientation further suggests that the 'duty cycle' that we introduced in BH10 may also be interpreted as an orientation effect, with only a certain fraction of haloes seen at an orientation where the observed flux exceeds the detection limit; Zheng et al. (2010) also consider this idea. A rather large sample of haloes would be required to determine the probability distribution of the observed Lyα flux from a halo of given mass and intrinsic luminosity. As briefly mentioned but not investigated in detail here, there should, however, obviously be also a variation of the spectral shape and surface brightness distribution with time in particular when a galaxy undergoes a major merger and/or starburst.

5.1 Limitations of the modelling

We will discuss now again in more detail some of the limitations of our modelling. First, the failure of the simulations of Tescari et al. (2009) to reproduce the high-velocity tail of the velocity width distribution of the associated metal absorption in DLAs suggests that higher outflow velocities, a more extended spatial distribution of the neutral gas, *and/or* a less clumpy and more spatially extended distribution of low-ionization metals are required from our galactic wind implementations. The effect of higher outflow velocities on the Lyα emission depends on exactly how the velocity would be increased. If the bulk velocity in the centre of the halo is increased, then this would accelerate frequency-space diffusion resulting in a more centrally peaked surface brightness profile. On the other hand, if the bulk velocity is increased primarily in the outer parts of the halo, then this would have a minimal effect, perhaps shifting photons back towards line centre and thereby increasing the apparent size of the emitter.

We have also not attempted to model the effects of dust on the Lyα radiation. DLAs are known to be among the most metal-poor systems in the high-redshift Universe, and are thus expected to be relatively dust free (Pontzen & Pettini 2009), apart from perhaps the most metal-rich systems (Fynbo et al. 2010, 2011). The long random walk of a typical Lyα photon makes them particularly susceptible to even a small amount of dust (Neufeld 1991; Laursen, Sommer-Larsen & Andersen 2009b).

Another worry could be our use of a rather coarse regular grid. Small-scale inhomogeneities in the H I density are, however, not likely to have much effect in the absence of dust. As we have seen the Lyα emission profile smoothes them over. At most, an irregular edge of an H I region may lead to a shallower surface brightness profile. Inhomogeneities in the bulk velocity would have a somewhat greater effect, increasing the frequency diffusion. These inhomogeneities could be modelled as a turbulent velocity, which has a similarly small effect as raising the temperature.

The fact that we have simply injected Lyα photons at the centre of the halo is a rather strong albeit observationally motivated assumption. Wolfe & Chen (2006) placed limits on the spatial extent of *in situ* star formation in DLAs, concluding that extended sources (radius $\gtrsim$3 kpc, 0.4 arcsec) were very rare.[5] As R08 and BH09 have argued, Lyα emission in the systems we are considering is most likely to be powered by star formation, suggesting that their large observed sizes are the result of radiative transfer through the surrounding neutral gas. Our main focus here has been on whether such a scenario is indeed plausible. The fact that the H I density peaks very near the centre of the halo means that the majority of photons should be emitted near the centre of the halo, as we have assumed. Making the intrinsic Lyα emission more extended would obviously make the observed emission also more extended. A more realistic Lyα emissivity would need to consider the interaction of UV radiation from star formation with the surrounding H I, as well as the possible contribution from cooling radiation (Faucher-Giguère et al. 2010) and fluorescence due to the UV background and quasars (Cantalupo et al. 2005; Cantalupo, Porciani & Lilly 2008; Kollmeier et al. 2010). However, fluorescence is expected to contribute little to the Lyα emission from DLAs (R08), and cooling is likely to only be significant in massive haloes, which are not expected to host the bulk of the DLA population. While cooling radiation may not account for the bulk of DLA Lyα luminosity, it could still be a relevant factor in determining the observed size of the emitters, as the surface brightness of the cooling radiation may drop less rapidly towards large radii than the radiation scattered outwards from central star-forming regions (Dijkstra et al. 2006; Dijkstra & Loeb 2009b; Faucher-Giguère et al. 2010).

We have considered here a rather small sample of haloes, for several reasons. First, it allows us to discuss some of the many factors relevant for the complicated interpretation of the Lyα emission at length. Also, the simulations of Tescari et al. (2009) used a box size that was too small to produce large numbers of haloes with $M_v > 10^{10.5}\,\mathrm{M}_\odot$. This was necessary to give an acceptable resolution. Our work here should thus be seen as complementary to the work of BH10. Many of the assumptions made there are borne out in the simulations described here. The Lyα emitters have considerable spatial extent, and are larger than the corresponding DLA cross-section as Lyα photons can be effectively scattered by gas with column

[5] Some extended star formation has recently been detected (Rafelski, Wolfe & Chen 2010) – as discussed previously, we will investigate the effect of spatially extended Lyα sources in future work.

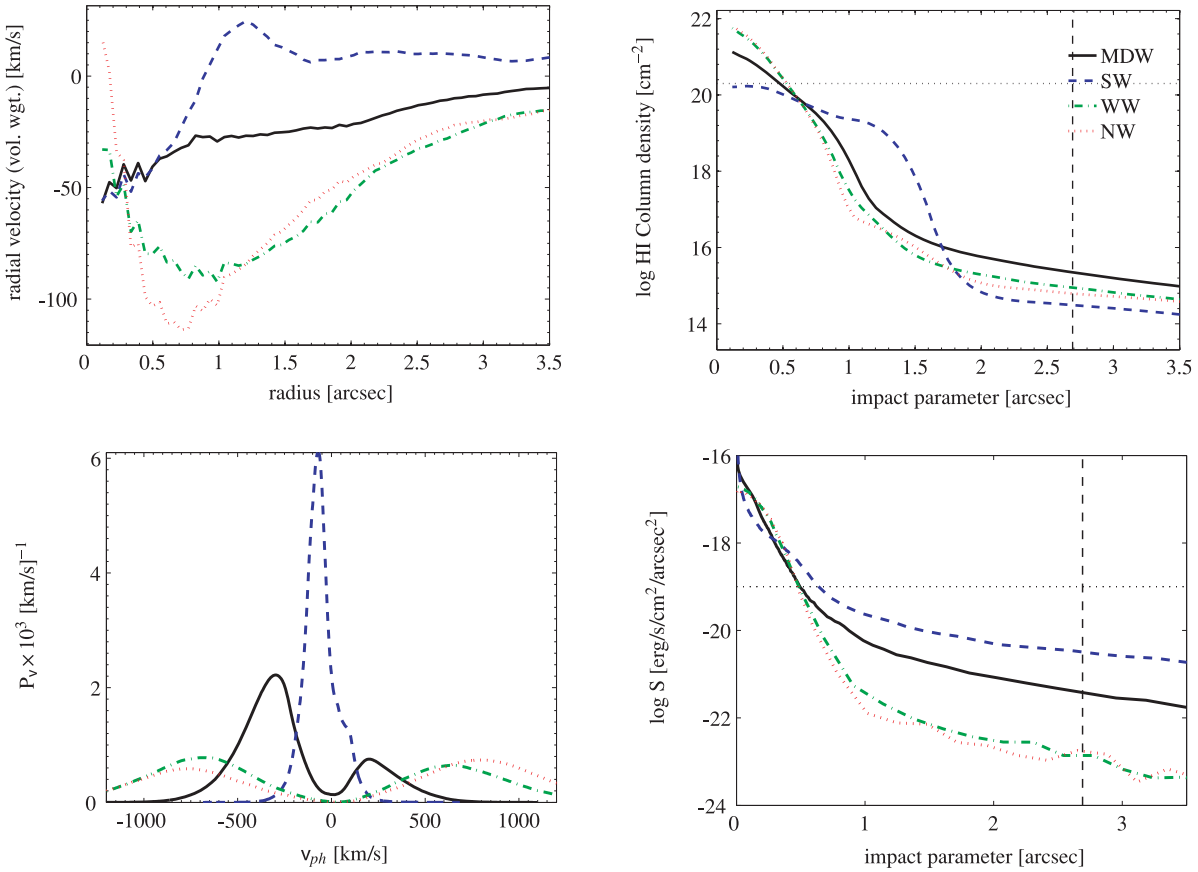

Figure 6. Angularly averaged properties of Halo 3, for the wind prescriptions shown in the legend (upper left), as discussed in Section 4.3. The panels plot the same quantities as in Fig. 5.

densities less than that of a DLA; the spectra are often double-peaked, with inflow/outflow producing a dominant blue/red peak; the radial velocity and mass flow rate are quite moderate towards the centre of the halo, increasing the spatial extent of the Lyα emission.

5.2 Relation to LBGs

Observationally, well-studied LBGs at similar redshift – presumably the more luminous and more massive cousins of typical DLA host galaxies – offer the opportunity to investigate their Lyα emission in considerably more detail, though a comparison may be hampered due to the increased role of dust and the fact that galactic winds are likely to be more powerful in these rapidly star-forming galaxies. Steidel et al. (2010) have summarized the properties of the observed Lyα emission in LBGs. Lyα is seen in emission and absorption with a wide range of equivalent width (EW). When observed in emission, Lyα typically shows a dominant red peak with offsets in the range of 200–800 km s^{-1} with respect to the systemic redshift as defined by the nebular emission lines. The medium offset of the Lyα emission is 485 $\pm$ 175 km s^{-1} with a typical width of 500 km s^{-1} (e.g. Quider et al. 2009). While the Lyα emission is offset towards the red, the interstellar absorption lines are offset to the blue with a mean of about -250 km s^{-1} and a tail of absorption often extending out to -800 km s^{-1}. In particular, the blueshift of the interstellar absorption line has been convincingly interpreted as being due to outflowing gas moving towards the observer (Verhamme, Schaerer & Maselli 2006). The most massive of our three haloes has a mass which is approaching that inferred for LBGs dark matter (DM) haloes, so it is interesting to see how our simulations compare. It is the momentum wind-driven model with its pronounced red peak which appears to have the most similar spectral distribution. The peak of the angular averaged emission in the MDW model is at about +400 km s^{-1}. The secondary blue peak is, however, considerably stronger than in the composite spectrum presented in Steidel et al. (2010), perhaps indicating that the central column density is somewhat too large and that real galactic winds in LBGs are more efficient in reducing the central optical depth. In fact, most LBGs do not show an intrinsic damped absorption system in their spectra and the outflow velocities indicated by the interstellar absorption lines appear to be higher than that of the outflowing gas in our simulations.

5.3 A more detailed comparison with the Rauch et al. emitters

We come now to a more detailed comparison with the R08 emitters. As discussed in R08 (see also BH10), for 12 of the 27 spectra only a single emission peak is visible while six/three of the spectra show a weak secondary blue/red counter-peak. The remaining spectra are extended in frequency space without a clear peak structure. The widths of the spectral peaks ranges from ∼250 to 1000 km s^{-1}. The surface brightness profiles are predominantly centrally peaked with wings that often extend well beyond the Gaussian core of the point spread function. This is particularly true of the brightest sources, while the fainter sources are more difficult to characterize due to the noise. As discussed in detail in Section 4, for the weak and NW model the spectral distribution shows rather symmetric

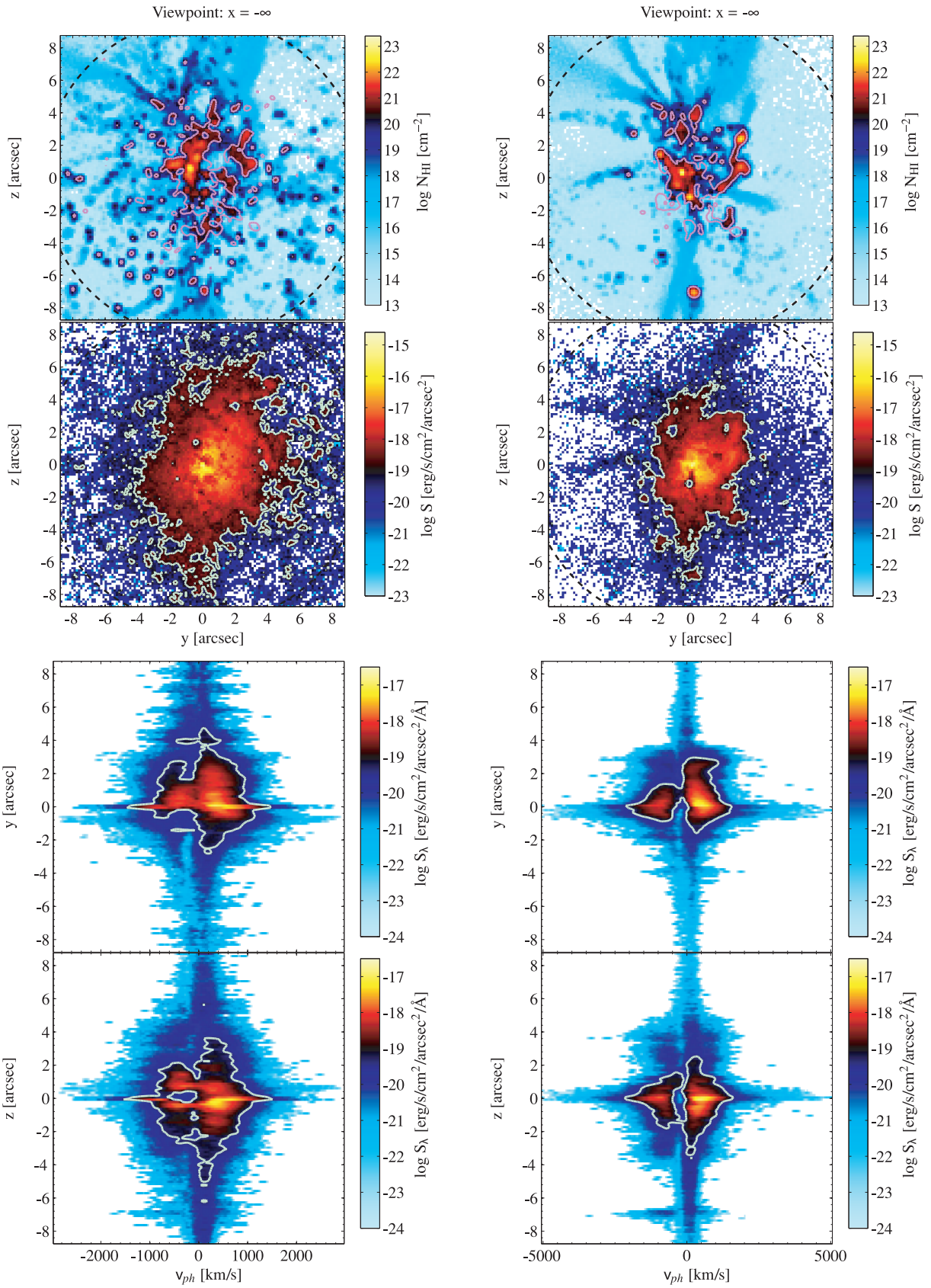

Figure 7. 2D images and spectra for the MDW (left) and WW (right) wind prescriptions for Halo 1 viewed from $x = -\infty$. The panels are the same as in Fig. 3. This figure is discussed further in Section 4.3.

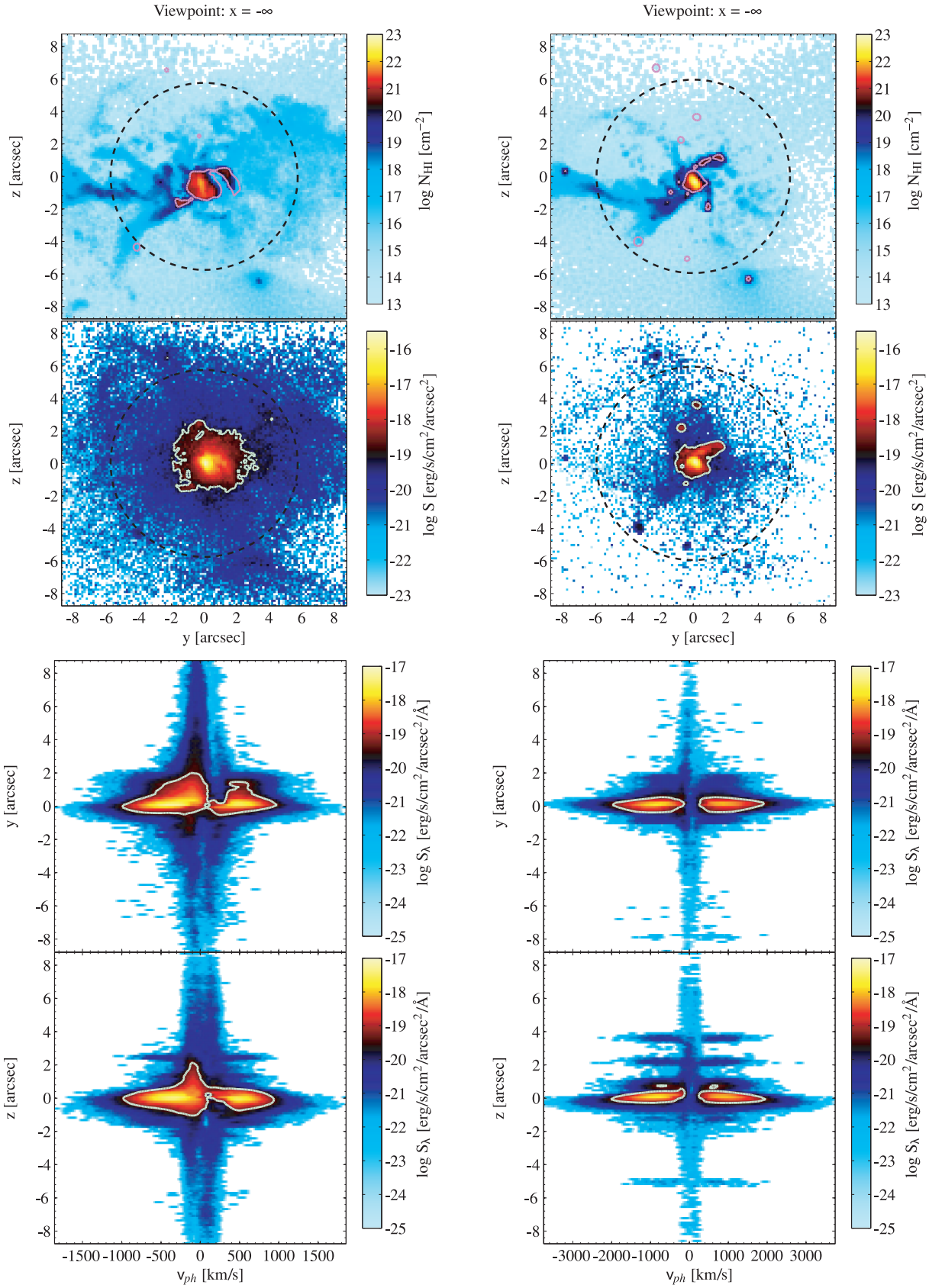

Figure 8. 2D images and spectra for the MDW (left) and WW (right) wind prescriptions for Halo 2 viewed from $x = -\infty$. The panels are the same as in Fig. 3. This figure is discussed further in Section 4.3.

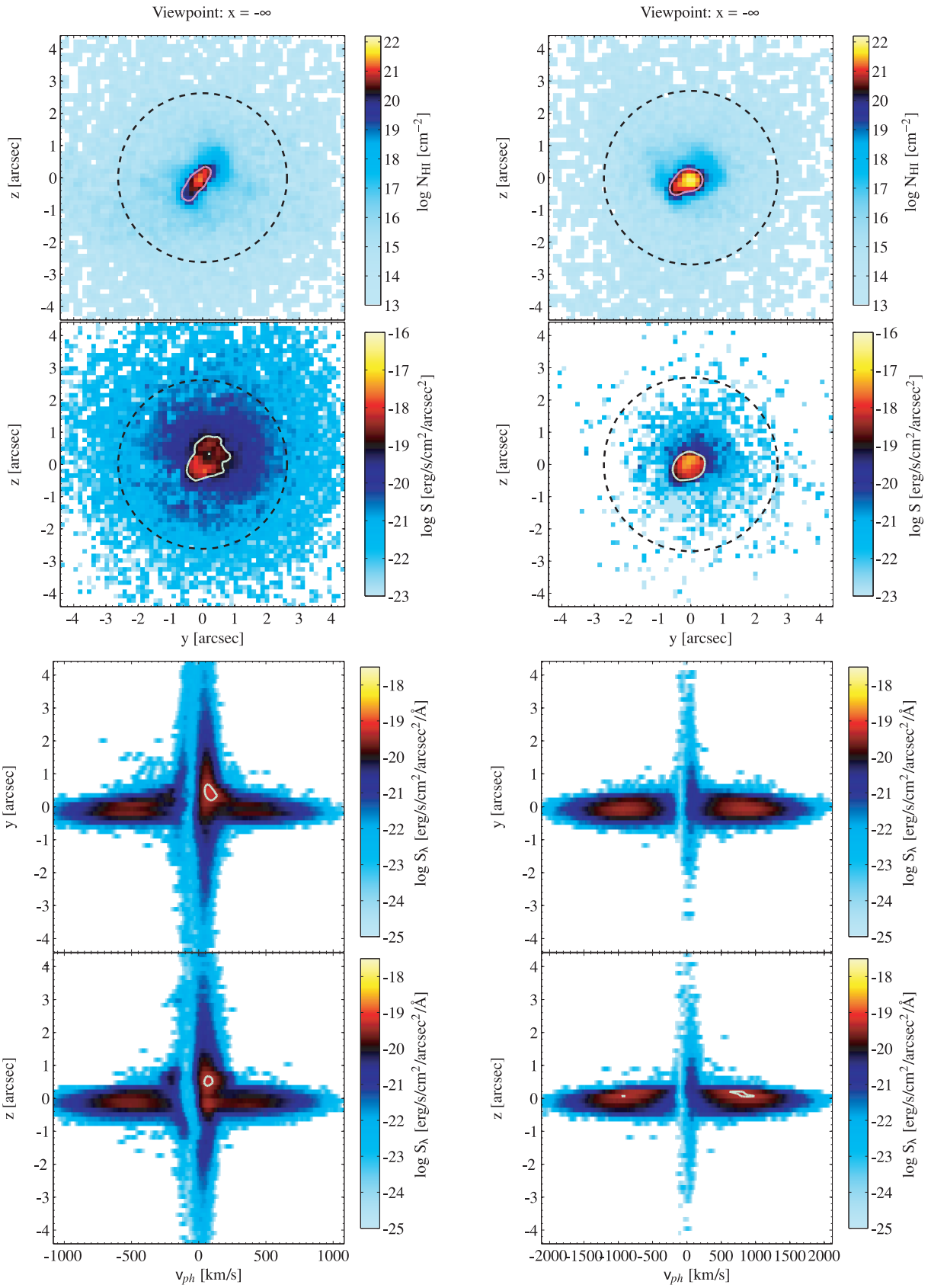

Figure 9. 2D images and spectra for the MDW (left) and WW (right) wind prescriptions for Halo 3 viewed from $x = -\infty$. The panels are the same as in Fig. 3. This figure is discussed further in Section 4.3.

double-peaked profiles. The R08 emitters appear instead to be similar to the two models with the stronger winds. Of the two models with SWs, the MDW model shows the more pronounced preference for a dominant red peak and generally the contrast between the two peaks is largest in this model. This model is thus probably the one which comes closest to the observed emitters. As discussed, the main difference between the models with the different wind implementations is due to the reduction of the central column density of neutral hydrogen due to the effect of the galactic wind. Note that most of the R08 emitters are only just above the detection threshold and offer thus a somewhat limited dynamic range. A weaker second peak would probably not be detected in many of the observed single-peak emitters. There is, however, a noticeable difference: some of the R08 emitters have more than one peak in the spatial direction, suggesting a more spatially extended source of ionizing photons perhaps with several peaks. As discussed previously, in our simulation the photons were all injected at the centre of the DM halo. As is apparent from the H I column density maps, the H I distribution is actually also rather clumpy. In a more quantitative study of a larger sample of haloes it would thus certainly be worthwhile to test if the correspondence between observation and simulations can be improved by injecting Lyα photons in several H I density peaks.

5.4 Implication for the detectability of faint high-redshift Lyα emitters

The velocity shift of Lyα emission due to resonant scattering is very important for the detectability of Lyα emitters at high redshift (e.g. Santos 2004). As hydrogen becomes increasingly neutral at high redshift, the optical depth to Lyα scattering due to the neutral IGM between the emitters and the observers steadily increases. As discussed e.g. by Zheng et al. (2010), Dijkstra & Wyithe (2010) and Laursen, Sommer-Larsen & Razoumov (2011), the effective transmission thereby depends sensitively on the optical depth to Lyα scattering and the details of the gas velocities within the emitter and the intervening IGM. Velocity shifts of about $500\,\mathrm{km\,s^{-1}}$ as observed in $z \sim 3$ LBG/Lyα emitters (LAEs) would strongly increase the transmission, which for appreciable shifts to the red scales as (Miralda-Escude 1998; Dijkstra, Lidz & Wyithe 2007; Dijkstra & Wyithe 2010), $\tau(\Delta v) \approx 2.7 x_{\rm H\,I} (\frac{\Delta v}{300\,\mathrm{km\,s^{-1}}})^{-1} (\frac{1+z}{7})^{3/2}$. Our modelling for the much fainter R08 emitters still suggests shifts of about $300\,\mathrm{km\,s^{-1}}$ which is good news for the detectability of faint Lyα emitters at high redshift perhaps even before reionization is complete. Note, however, that in our model the shift towards the red decreases rather than increases with increasing strength of galactic winds. As discussed in Section 4, this reduced shift towards the red is due to the decreased central column density of neutral hydrogen in the models with the stronger galactic winds. For a good estimate of the expected velocity shift it should thus be more important to predict the correct column density than the exact outflow velocity of the gas.

6 CONCLUSIONS

We have used here realistic numerical simulations of DLA host galaxies including the effect of galactic winds to investigate the spatial and spectral distribution of low surface brightness Lyα emission assuming that the emission is powered by star formation at the centre of the corresponding DM haloes. Our main results can be summarized as follows.

(i) The haloes contain a mixture of inflowing and outflowing gas. As a result, the angularly averaged spectrum typically shows two peaks, with the relative strength of the red (blue) peak being a reflection of the relative contribution of outflow (inflow) as characterized by the volume-weighted radial velocity of H I. The separation of the two peaks is mainly governed by the central H I column density. Line-centre photons can escape due to inhomogeneities in the gas density providing low-density paths of escape and bulk velocities allowing rapid diffusion in the fluid frame frequency space. The different wind implementations lead to significantly different central H I column densities as well as different radial motions of the gas, which are reflected in different spectral shapes of the Lyα emission.

(ii) A comparison of the 2D column density and surface brightness images shows that the Lyα emission region is larger and smoother than the cross-section for damped absorption. Lyα photons escaping at large radii illuminate regions of protogalaxies that would be probed by absorption line spectra with column densities down to $N_{\rm H\,I} \sim 10^{18}\,\mathrm{cm^{-2}}$ and below. The central source can effectively light up outlying clumps of neutral hydrogen. Asymmetries in the H I distribution can dramatically affect the observed surface brightness, with dense clumps casting shadows as photons are reflected off their surface. A central source of photons can illuminate diffuse, highly ionized gas inside and beyond the virial radius at very faint surface brightness levels.

(iii) The 2D spectra show considerable variety for the same halo viewed from different angles. A typical line profile is double-peaked with one of the peaks dominating. The separation of the peaks decreases with increasing distance from the central, dense regions of the halo. The dominance of the red or blue peak changes with the viewing angle, and is affected by the velocity of the gas relative to the observer. The maximum spectral intensity is approximately constant across the different haloes at $S_\lambda \approx 10^{-17.5}$ $\mathrm{erg\,s^{-1}\,cm^{-2}\,arcsec^{-2}\,\AA^{-1}}$, with the decrease in luminosity with mass being countered by reduced spatial and frequency diffusion.

(iv) The angularly averaged surface brightness profile is most sensitive to the column density of the gas at the centre of the haloes which in turn is very sensitive to the feedback from galactic winds. The more efficient feedback implementations result in reduced column densities at the centre and therefore reduced diffusion in frequency space and narrower spectral profiles. The maximum blue/redshift in our emitters is also primarily sensitive to the central H I column density and not the velocity of the wind. For objects with column densities and wind velocities similar to those in our simulations, galactic winds may in fact reduce rather than increase the visibility of Lyα emitters during the epoch of reionization when the hydrogen in the IGM is not yet (fully) ionized and Lyα emission from galaxies is strongly suppressed due to the damping wing of the IGM's Gunn–Peterson trough.

(v) For the MDW model (and to a somewhat lesser extent also the SW implementation), our simulated emitters show encouraging agreement with the properties of the R08 emitters and thus further corroborate the suggestion that these are the long-sought host population of DLAs. This preference for the MDW models also appears to result in better agreement with a range of other observed properties of high-redshift galaxies and the IGM (Oppenheimer & Davé 2008). There are, however, at the same time differences between observed and simulated emitters. The simulated spectra do not show quite the preference for a dominant red peak the observed emitters appear to suggest. This is partially due to the fact that we have not modelled the impact of the intervening IGM which will reduce the observed emission in the blue peak relative to the red peak. Our investigation nevertheless appears to suggest that somewhat larger outwards motion are required than present in our

MDW simulations where especially in the smaller haloes the feedback due to the galactic winds is not quite sufficient to globally reverse the infall of gas. This may well be related to the fact that the simulations also struggle to reproduce the tail of high-velocity widths for the associated low-ionization absorption of DLAs. The existence of several clumps in the observed Lyα emission further suggests that the emissivity of ionizing photons is more spatially extended than the central injection we have assumed in our simulations.

The study of the effect of galactic winds in a cosmological galaxy formation simulation presented here contributes further to unravelling the complexities of the Lyα emission from high-redshift galaxies. The rather strong dependence of the Lyα emission on the details of the wind implementation should allow spatially extended low surface brightness Lyα emission to be turned into an important diagnostic tool for studying the internal dynamics of galactic winds as well as their effect on the interstellar and circumgalactic medium of high-redshift galaxies.

ACKNOWLEDGMENTS

We thank Michael Rauch, George Becker, Sebastiano Cantalupo, Mark Dijkstra, Max Pettini, Dan Stark, Bob Carswell and Richard Bower for helpful discussions. We also thank Luca Tornatore for allowing us to use his modified version of GADGET-2 to run simulations.

MGH was partially supported by STFC grant LGAG 092/RG43335. LAB was supported by an Overseas Research Scholarship and the Cambridge Commonwealth Trust, and the Swiss National Science Foundation (SNSF). MV is supported by PRIN/INAF, ASI/AAE grant, INFN PD/51 and by the ERC Starting Grant 'cosmoIGM'. ET acknowledges a fellowship from the European Commission's Framework Programme 7, through the Marie Curie Initial Training Network CosmoComp PITN-GA-2009-238356. Numerical computations were done on the COSMOS (SGI Altix 3700) supercomputer at DAMTP, the High Performance Computer Cluster (HPCF) in Cambridge (UK) and at Centro Interuniversitario del Nord Est per il Calcolo Elettronico (CINECA), Italy. COSMOS is a UK-CCC facility which is supported by HEFCE, PPARC and Silicon Graphics/Cray Research. The CINECA CPU time has been assigned thanks to an INAF-CINECA grant.

REFERENCES

Barnes L. A., 2010, PhD thesis, Univ. Cambridge
Barnes L. A., Haehnelt M. G., 2009, MNRAS, 397, 511
Barnes L. A., Haehnelt M. G., 2010, MNRAS, 403, 870
Cantalupo S., Porciani C., Lilly S. J., Miniati F., 2005, ApJ, 628, 61
Cantalupo S., Porciani C., Lilly S. J., 2008, ApJ, 672, 48
Cen R., 2010, preprint (arXiv:1010.5014)
Cowie L. L., Hu E. M., 1998, AJ, 115, 1319
Dijkstra M., Loeb A., 2009a, MNRAS, 396, 377
Dijkstra M., Loeb A., 2009b, MNRAS, 400, 1109
Dijkstra M., Wyithe J. S. B., 2010, MNRAS, 1158
Dijkstra M., Haiman Z., Spaans M., 2006, ApJ, 649, 14
Dijkstra M., Lidz A., Wyithe J. S. B., 2007, MNRAS, 377, 1175
Faucher-Giguère C.-A., Kereš D., Dijkstra M., Hernquist L., Zaldarriaga M., 2010, ApJ, 725, 633
Finkelstein S. L. et al., 2010, preprint (arXiv:1008.0634)
Fynbo J. P. U. et al., 2010, MNRAS, 408, 2128
Fynbo J. P. U. et al., 2011, MNRAS, 413, 2481
Haehnelt M. G., Steinmetz M., Rauch M., 1998, ApJ, 495, 647
Haehnelt M. G., Steinmetz M., Rauch M., 2000, ApJ, 534, 594
Harrington J. P., 1973, MNRAS, 162, 43
Hayashino T. et al., 2004, AJ, 128, 2073
Hong S., Katz N., Davé R., Fardal M., Kereš D., Oppenheimer B. D., 2010, preprint (arXiv:1008.4242)
Hu E. M., Cowie L. L., McMahon R. G., Capak P., Iwamuro F., Kneib J.-P., Maihara T., Motohara K., 2002, ApJ, 568, L75
Iye M. et al., 2006, Nat, 443, 186
Kashikawa N. et al., 2006, ApJ, 648, 7
Kodaira K. et al., 2003, PASJ, 55, L17
Kollmeier J. A., Zheng Z., Davé R., Gould A., Katz N., Miralda Escudé J., Weinberg D. H., 2010, ApJ, 708, 1048
Laursen P., Razoumov A. O., Sommer-Larsen J., 2009a, ApJ, 696, 853
Laursen P., Sommer-Larsen J., Andersen A. C., 2009b, ApJ, 704, 1640
Laursen P., Sommer-Larsen J., Razoumov A. O., 2011, ApJ, 728, 52
Maller A. H., Bullock J. S., 2004, MNRAS, 355, 694
Miralda Escude J., 1998, ApJ, 501, 15
Neufeld D. A., 1990, ApJ, 350, 216
Neufeld D. A., 1991, ApJ, 370, L85
Oppenheimer B. D., Davé R., 2008, MNRAS, 387, 577
Ota K. et al., 2008, ApJ, 677, 12
Ouchi M. et al., 2010, ApJ, 723, 869
Pontzen A., Pettini M., 2009, MNRAS, 393, 557
Pontzen A. et al., 2008, MNRAS, 390, 1349
Quider A. M., Pettini M., Shapley A. E., Steidel C. C., 2009, MNRAS, 398, 1263
Rafelski M., Wolfe A. M., Chen H.-W., 2010, preprint (arXiv:1011.6390)
Rauch M. et al., 2008, ApJ, 681, 856
Razoumov A. O., Norman M. L., Prochaska J. X., Sommer-Larsen J., Wolfe A. M., Yang Y.-J., 2008, ApJ, 683, 149
Rhoads J. E. et al., 2004, ApJ, 611, 59
Santos M. R., 2004, MNRAS, 349, 1137
Springel V., 2005, MNRAS, 364, 1105
Springel V., Hernquist L., 2003, MNRAS, 339, 289
Stanway E. R. et al., 2007, MNRAS, 376, 727
Steidel C. C., Adelberger K. L., Shapley A. E., Pettini M., Dickinson M., Giavalisco M., 2000, ApJ, 532, 170
Steidel C. C., Erb D. K., Shapley A. E., Pettini M., Reddy N., Bogosavljević M., Rudie G. C., Rakic O., 2010, ApJ, 717, 289
Taniguchi Y. et al., 2005, PASJ, 57, 165
Tasitsiomi A., 2006, ApJ, 645, 792
Tescari E., Viel M., Tornatore L., Borgani S., 2009, MNRAS, 397, 411
Tescari E., Viel M., D'Odorico V., Cristiani S., Calura F., Borgani S., Tornatore L., 2011, MNRAS, 411, 826
Tornatore L., Borgani S., Dolag K., Matteucci F., 2007, MNRAS, 382, 105
Tornatore L., Borgani S., Viel M., Springel V., 2010, MNRAS, 402, 1911
Urbaniak J. J., Wolfe A. M., 1981, ApJ, 244, 406
Verhamme A., Schaerer D., Maselli A., 2006, A&A, 460, 397
Wolfe A. M., Chen H.-W., 2006, ApJ, 652, 981
Wood K., Reynolds R. J., 1999, ApJ, 525, 799
Yusef-Zadeh F., Morris M., White R. L., 1984, ApJ, 278, 186
Zheng Z., Cen R., Trac H., Miralda Escudé J., 2010, ApJ, 716, 574
Zheng Z., Cen R., Trac H., Miralda Escudé J., 2011, ApJ, 726, 38

This paper has been typeset from a TEX/LATEX file prepared by the author.